CHAPTER 3

COMPARISON OF ATTENUATION-COMPENSATION FUNCTIONS

In Chapter 2, the backscattered voltage from a region of homogeneous scatterers and from a rigid plane placed near the focus was rederived. These calculations demonstrated that focusing along the beam axis can be corrected by using a generalized attenuation-compensation function, A_{comp}. The equations also indicated that for focused sources, O'Donnell-Miller compensation, A_{OM}, should result in an overestimate of the scatterer size, and point compensation, A_{PC}, may either overestimate or underestimate the scatterer size depending on the degree of focusing and amount of attenuation. However, the overall estimation performance was not quantified. Therefore, in this chapter, a series of simulations and phantom experiments are presented to quantify the performance of the different attenuation-compensation functions similar to the study done by *Oelze and O'Brien* [2002a]. In their work, they introduced a new attenuation-compensation function, denoted Oelze-O'Brien compensation, given by

$$A_{OO}(\omega) = \frac{e^{4\alpha_{eff} z_T}\, e^{-4\alpha\frac{L}{2}}}{L}\left(\frac{2\alpha L}{1-e^{-2\alpha L}}\right)^2, \tag{3.1}$$

which they found underestimated the scatterer size for the unfocused source. Therefore, their attenuation-compensation function was also considered in our analysis. A_{OO} cannot be derived from Equation (2.51) because the derivation dealt with the $E\left[\left|V_{refl}(\omega)\right|^2\right]$, whereas A_{OO} was originally derived for $\left(E\left[\left|V_{refl}(\omega)\right|\right]\right)^2$. The analysis in this chapter also considered the effects of window length, attenuation, focusing, and scatterer type.

3.1 Simulation Analysis of Gaussian Scatterers

In the initial analysis, the scatterers had a spherical Gaussian impedance distribution (Gaussian scatterers). The sources were assumed to be spherically focused transducers with their apertures placed in contact with an attenuating infinite half-space (infinite region bounded by aperture plane of source) containing scatterers. The transducers were excited by an impulse spike and had filtering characteristics $H(f)$ given by

$$H(f) = \frac{|f| \cdot \exp\left(-\left(\frac{f - 8\,\text{MHz}}{6\,\text{MHz}} \right)^2 \right)}{\max\limits_{\forall f}\left(f \cdot \exp\left(-\left(\frac{f - 8\,\text{MHz}}{6\,\text{MHz}} \right)^2 \right) \right)}, \tag{3.2}$$

which was comparable to a single-element transducer in our laboratory. A Rayleigh distribution was selected over a Gaussian distribution so that nothing would be transmitted/received at zero frequency just like the filtering characteristics of a real source. Also, the sources had a focal length of 5 cm and f-numbers of 1, 2, and 4. The velocity potential field at the focus in the simulations had a three-dimensional Gaussian distribution (i.e., only approximation of field for focused source) with G_o, w_x, w_y, and w_z given by

$$G_o = \frac{F}{8(f\#)^2} \tag{3.3}$$

and

$$\begin{aligned} w_x &= w_y = 0.87\lambda f\# \\ w_z &= 6.01\lambda(f\#)^2 \end{aligned}, \tag{3.4}$$

where F is the focal length and $f\#$ is the f-number of the source.

The backscattered voltage for the simulations was generated by solving Equation (2.34) analytically for a single Gaussian scatterer at an arbitrary location in the Gaussian field of the focal region. The backscattered voltage from many scatterers in the half-space was then obtained by adding together the backscattered voltage from many different randomly distributed scatterers as is described in Appendix D. In the simulations, the scatterers were positioned according to a uniform probability distribution throughout the focal region at a density of 35/mm^3 and each had an effective radius a_{eff} of 25 μm.

A density of 35/mm^3, given that the approximate length of the transmitted pulse was ~0.286 mm, translates to 4.8, 1.2, and 0.3 scatterers per resolution cell in the B-mode image for

the *f*/4, *f*/2, and *f*/1, respectively. Hence, the speckle would not be fully developed in a B-mode image from the *f*/1 and *f*/2 transducers. This is of little concern because it is the overall shape of the frequency spectrum and not the speckle that is being analyzed. As a result, a fully developed speckle pattern is not needed to perform the analysis. To verify this assertion, the number density of the scatterers was varied from 35/mm^3 to 3500/mm^3 for the *f*/1 transducer. The accuracy of the scatterer size estimates was the same for all of the number densities (~1%). The precision of the estimates was improved for larger number densities (from ~26% to ~15%), but the amount of improvement did not warrant an increase in the number density for the simulations.

The sound speed for the half-space was 1532 m/s, which is the sound speed of liver (characteristic of tissue). The attenuation was uniform throughout the half-space for each simulation and was varied from 0.05 to 1 dB/cm/MHz for different simulations. The reflection off of the rigid plane at the focus in a water bath was also simulated according to Equation (2.71) using a constant sound speed of 1540 m/s and setting $z_f = 0$. The code used a sampling rate of 53 MHz when "digitizing" the signal significantly over sampling the waveform, and no electronic noise was added to the simulated waveforms.

For each value of attenuation, the backscattered voltage from 1000 independent random scatterer distributions was generated. The waveforms were then separated into 40 independent sets with 25 waveforms per set and windowed in the time domain using a rectangular gating function centered at the focus. The width of the rectangular window was varied from 1 mm to 13 mm in steps of 1 mm with time gates found from $T_{win} = 2L/c$. Then, $\mathrm{E}\left[\left|V_{refl}(\omega)\right|^2\right]$ was calculated by averaging the magnitude squared of the frequency spectrum of the 25 signals. Equation (2.75) was then solved by minimizing the squared error yielding 40 independent estimates of the effective scatterer radius $a_{eff\,j}$. In all cases, the bandwidth selected for the minimization was the set of frequencies for which

$$\frac{k_o^4\, \mathrm{e}^{-4\alpha z_T}\left|V_{plane}(\omega)\right|^2}{\max\limits_{\forall \omega}\left(k_o^4\, \mathrm{e}^{-4\alpha z_T}\left|V_{plane}(\omega)\right|^2\right)} > 0.05. \tag{3.5}$$

The results for an attenuation of 0.5 dB/cm/MHz for all three transducers (i.e., *f*/1, *f*/2, and *f*/4) and all window lengths are shown in Figures 3.1, 3.2, and 3.3. In Figure 3.1, the percent

error in the scatterer size is compared to the known size for the three transducers for each of the different attenuation-compensation functions. The upper and lower error bars were found from

$$\sigma_{a_{upper}} = \frac{100}{a_{eff}\big|_{Theory}} \sqrt{\frac{\sum_{\forall a_{eff\,j} > \bar{a}_{eff}} \left(a_{eff\,j} - \bar{a}_{eff}\right)^2}{\sum_{\forall a_{eff\,j} > \bar{a}_{eff}} j}} \quad \sigma_{a_{lower}} = \frac{100}{a_{eff}\big|_{Theory}} \sqrt{\frac{\sum_{\forall a_{eff\,j} < \bar{a}_{eff}} \left(a_{eff\,j} - \bar{a}_{eff}\right)^2}{\sum_{\forall a_{eff\,j} < \bar{a}_{eff}} j}}. \quad (3.6)$$

The accuracy of all estimates drops off significantly at smaller window lengths for all of the attenuation-compensation functions as a result of the convolution in the frequency domain associated with the windowing.

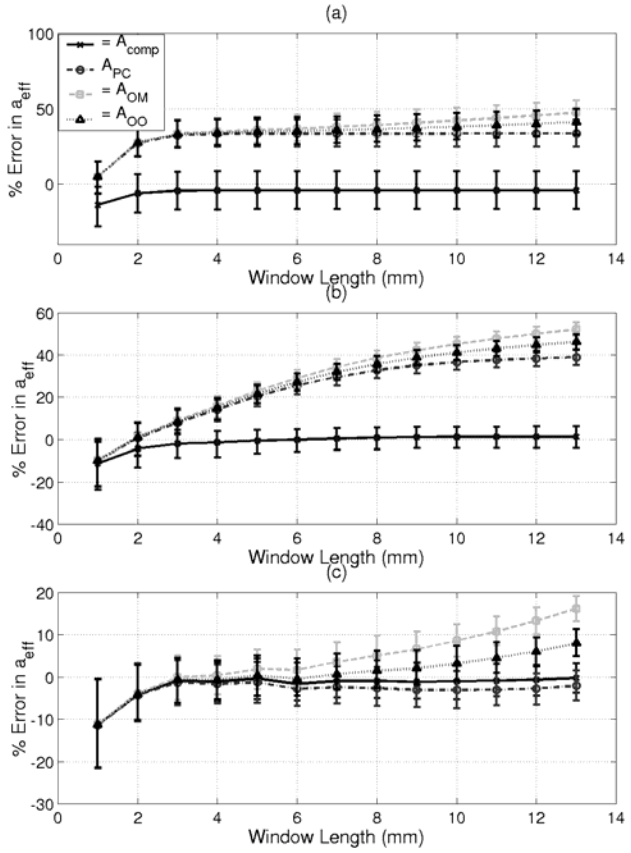

Figure 3.1: Percent error vs. rectangular window length when compared to known a_{eff} at $\alpha = 0.5$ dB/cm/MHz for simulated fields from (a) *f*/1 (b) *f*/2, and (c) *f*/4 transducers.

In Figure 3.2, the percent difference between the scatterer size given by the generalized attenuation-compensation function A_{comp}, and the scatterer size from the other attenuation-compensation functions are compared for the three transducers. It is clear that the error bars are

reduced when the difference between the attenuation-compensation functions are found (Figure 3.2) as compared to plotting the straight error values (Figure 3.1). Hence, the differences between the different attenuation-compensation functions should be relatively constant between different scatterer distributions even though the absolute errors vary. Figure 3.3 shows the percent differences again, but here the window length has been normalized with respect to the calculated depth of field for the transducer (i.e., $7.08\lambda_o f\#^2$) [*Kino*, 1987], where λ_o was the wavelength corresponding to the spectral peak from the reference spectrum (i.e., V_{plane}).

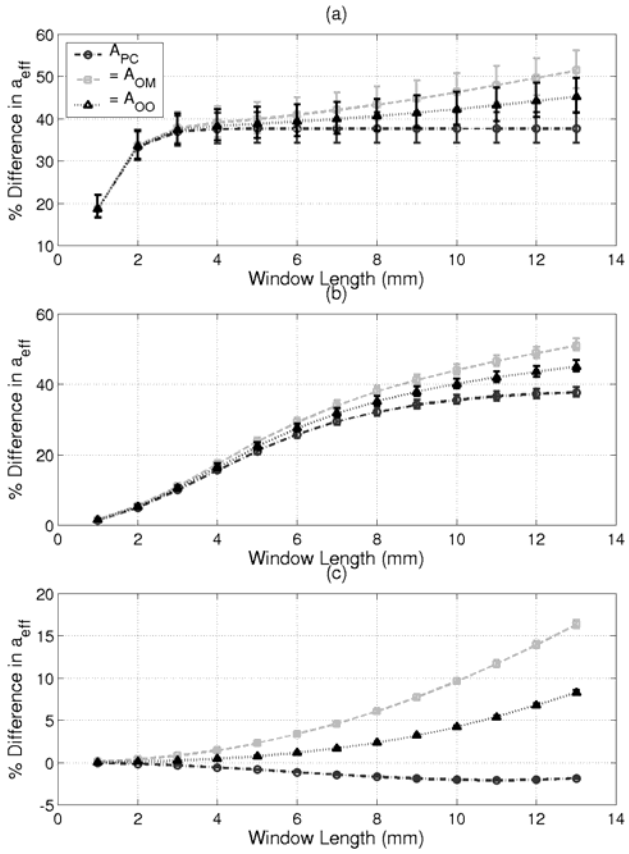

Figure 3.2: Percent difference vs. rectangular window length when compared to a_{eff} found using A_{comp} in Equation (2.51) at $\alpha = 0.5$ dB/cm/MHz for simulated fields from (a) *f*/1 (b) *f*/2, and (c) *f*/4 transducers.

The errors (Figure 3.1) and differences (Figure 3.2) in A_{OM}, A_{OO}, and A_{PC} are larger for the smaller f-number transducers (i.e., *f*/1 and *f*/2) and increase for longer window lengths. This makes sense because the importance of diffraction along the beam axis increases with increasing window length. Likewise, all four attenuation-compensation functions converge to the same

result for decreasing window lengths. *Oelze and O'Brien* [2002a] also observed this when diffraction along the beam axis was neglected. Furthermore, A_{comp} yields excellent results regardless of window length or f-number and even provides improved estimates for the scatterer size for long window lengths when the beam is relatively unfocused (i.e., *f*/4). Also, when the results for the *f*/1 and the *f*/2 transducers are compared, the errors/differences plateau with increasing window length. Hence, the differences are greater for the *f*/1 transducer for smaller window lengths and then are approximately the same for large window lengths.

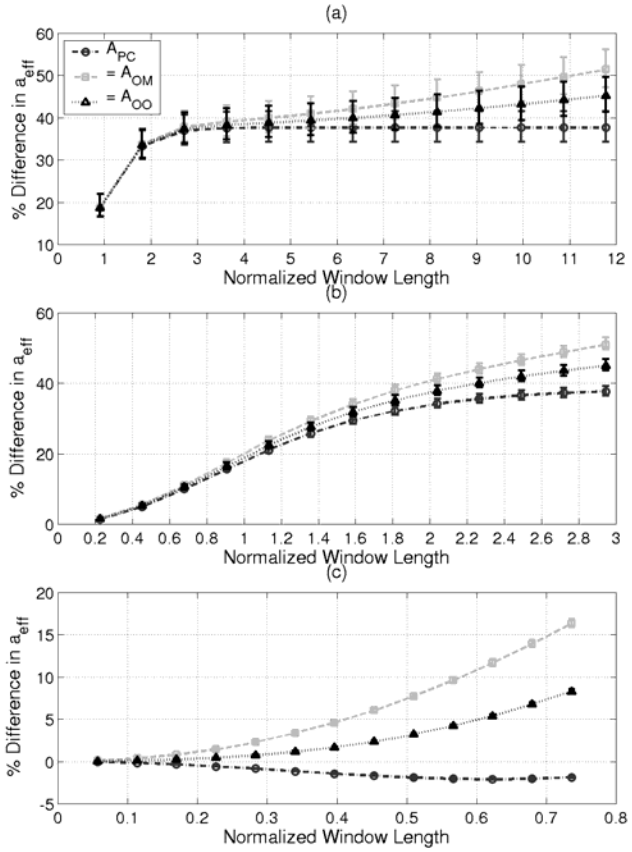

Figure 3.3: Percent difference vs. window length normalized to the depth of focus (i.e. $7.08\lambda_o f\#^2$) when compared to a_{eff} found using A_{comp} in Equation (2.51) at $\alpha = 0.5$ dB/cm/MHz for simulated fields from (a) *f*/1 (b) *f*/2, and (c) *f*/4 transducers.

The plateau can be better illustrated by the results for the normalized window lengths (Figure 3.3). The plateau is reached once the window length is several times the calculated depth of field; hence, the contributing scatterers are being limited by the focusing of the field and not by the windowing. Also, when comparing the differences between the *f*/1 and the *f*/2 transducers

at the same normalized window length, the *f*/2 transducer has a larger difference for both the A_{OM} and A_{OO} estimates, and the A_{PC} estimate values converge to the same difference of 37.6% for normalized window lengths greater than approximately 2.5. Likewise, when comparing the differences between the *f*/2 and the *f*/4 transducers at the same normalized window length, the *f*/4 transducer has a larger difference for the A_{OM} estimate. Also, for the *f*/4 transducer, the concavity of the A_{PC} estimate changed direction at a normalized window length of 0.65. Hence, A_{PC} may overestimate the scatterer size for large enough window lengths. Therefore, the error in using A_{OM} is greater for transducers with larger f-number when comparing across the same normalized window length, and the error in A_{PC} appears to plateau at sufficiently large normalized window length at approximately 37.6%. However, the performance of the attenuation-compensation functions cannot be generalized for small normalized window lengths for the different focused transducers.

The improvement in the estimates using the new generalized attenuation-compensation function can be illustrated further by considering the error in $\overline{a}_{eff}$ (average size estimate) for different values of attenuation at set rectangular window lengths of 6 and 13 mm (Figures 3.4 and 3.5, respectively). For the *f*/1 and *f*/2 transducers, A_{OM}, A_{OO}, and A_{PC} consistently overestimate the scatterer size on the order of 20% to 100%, while A_{comp} gives almost exactly the right answer with errors typically less than 2% with the largest error being 7.2%. However, for the *f*/4 transducer, although A_{OM} consistently overestimates the scatterer size, both A_{OO} and A_{PC} overestimate the scatterer size for small values of attenuation and then underestimate the scatterer size as the attenuation is increased. This is in agreement with *Oelze and O'Brien* [2002a] who also observed that A_{OM} should overestimate the scatterer size and both A_{OO} and A_{PC} should underestimate the scatterer size for long window lengths when diffraction along the beam axis can be neglected. The results for A_{PC} also agree with our predictions that A_{PC} will under/overestimate the scatterer size based on the relative importance of α and w_z. When focusing dominates, A_{PC} overestimates the scatterer size, and when attenuation dominates, A_{PC} underestimates the scatterer size. Once again, A_{comp} gives consistently good results for all attenuation values for the *f*/4 transducer with errors less than 5%. Hence, including diffraction along the beam axis with the generalized attenuation-compensation function improves the accuracy of the scatterer size estimate and allows for more strongly focused sources (i.e., *f*/1 and *f*/2) to be used in the data acquisition.

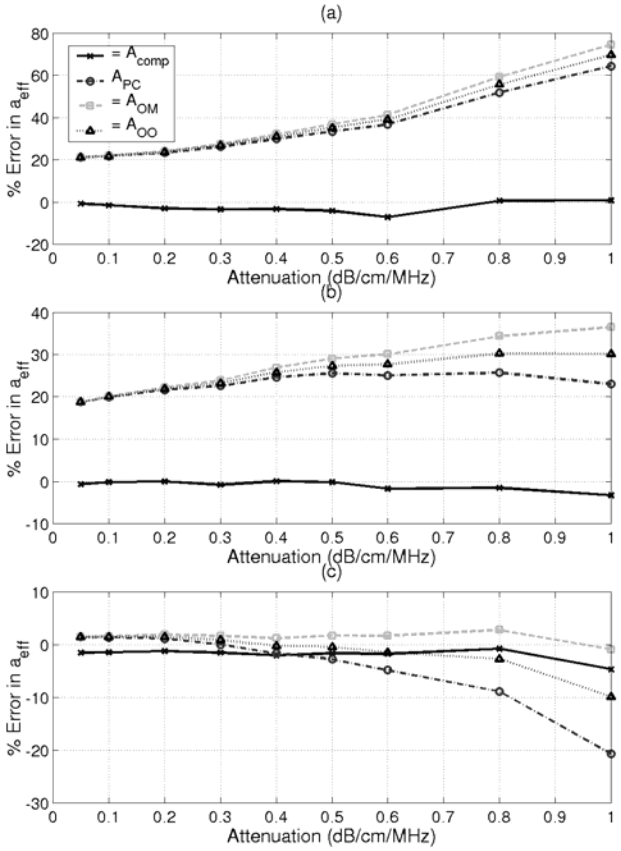

Figure 3.4: Percent error in $\overline{a}_{eff}$ when compared to known value of a_{eff} for L = 6 mm for simulated fields from (a) *f*/1, (b) *f*/2, and (c) *f*/4 transducers.

Although the accuracy of the scatterer size estimate is an important measure of the performance of the estimator, the precision of the estimate is also of great importance when performing tissue characterization. Figure 3.6 shows the deviations in the scatterer size calculated by averaging $\sigma_{a_{upper}}$ and $\sigma_{a_{lower}}$ from Equation (3.6) for each of the attenuation-compensation functions at a window length of 6 mm for all three of the transducers. Results at other window lengths are typically comparable to within a few percent. There is a slight degradation in the precision of the algorithms with increasing attenuation (i.e., change on the order of 8% from 0.05 dB/cm/MHz to 1 dB/cm/MHz) and with decreasing f-number (i.e., change on the order of 8% from *f*/1 to *f*/4). These losses in precision may be a result of having fewer scatterers contributing to the backscattered signal as well as having the ka_{eff} values shift out of the optimal range [*Insana and Hall*, 1990] of $ka_{eff} = 0.5 \rightarrow 1.2$ due to the increased attenuation

(i.e., from $ka_{eff} = 0.67 \rightarrow 1.6$ to $ka_{eff} = 0.26 \rightarrow 0.96$). More will be said on the effect of the ka_{eff} values in Chapter 7. Also, although the precision of the different attenuation-compensation functions are comparable, A_{comp} is slightly less precise than the other algorithms for the *f*/1 and *f*/2 transducers (i.e., change on the order of 1% to 7%). This loss in precision, however, is insignificant compared to the simultaneous gain in accuracy.

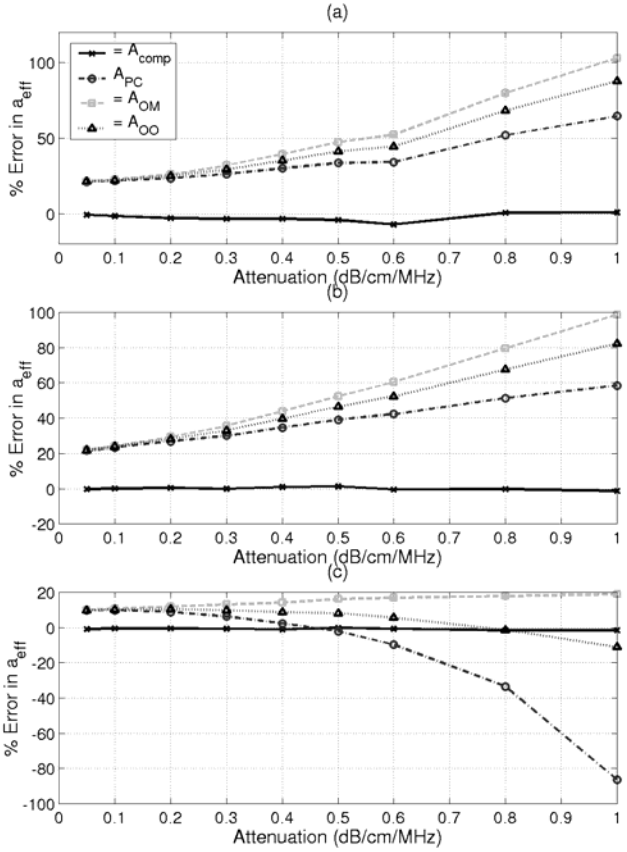

Figure 3.5: Percent error in $\overline{a}_{eff}$ compared to known value of a_{eff} for L = 13 mm for simulated fields from (a) *f*/1, (b) *f*/2, and (c) *f*/4 transducers.

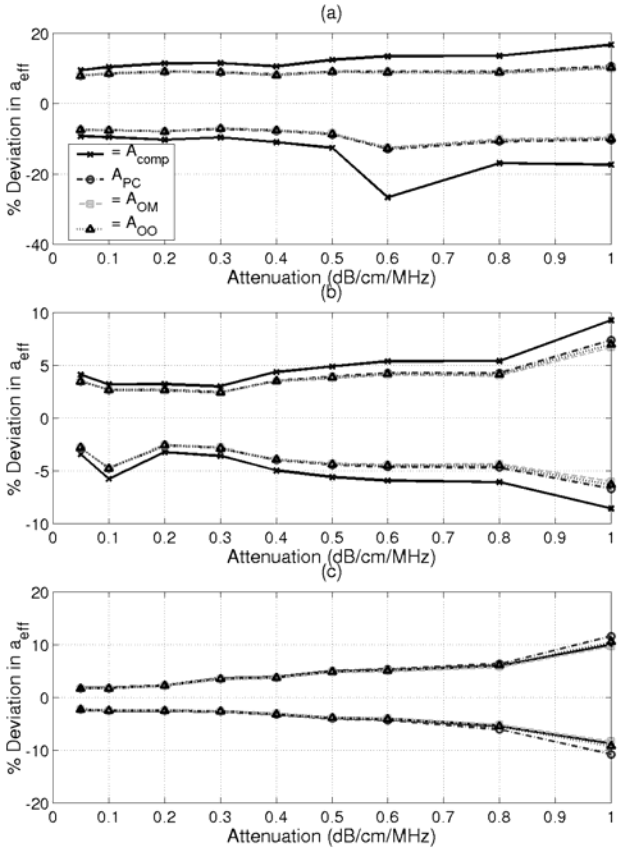

Figure 3.6: Percent deviations in a_{eff} for a window length of 6 mm for each of the attenuation-compensation functions for simulated fields from (a) *f*/1, (b) *f*/2, and (c) *f*/4 transducers. The upper curves in each plot are the values of $\sigma_{a_{upper}}$ and the lower curves in each plot are $\sigma_{a_{lower}}$.

3.2 Experimental Results for Glass Bead Scatterers

After the initial simulation study, the improvement provided by the new generalized attenuation-compensation function was validated experimentally. Before the experiment could be performed, the equivalent Gaussian dimensions (beamwidth and depth of focus) of the real focused sources had to be determined.

3.2.1 Equivalent Gaussian dimension measurement

There are many possible methods for determining the equivalent Gaussian dimensions of an ultrasound source, two of which were compared experimentally in the investigation. The evaluation was done using a spherically focused *f*/2 transducer (Valpey Fisher Instruments, Inc.,

Hopkinton, MA) with a diameter of 2.1 cm, a center frequency of 8.7 MHz, and a –3 dB bandwidth of 1.6 MHz as measured from a wire reflection [*Raum and O'Brien*, 1997]. The transducer was placed in a water bath and shock excited using a Panametrics 5900 pulser/receiver (Waltham, MA) operating in pulse-echo mode, and the returned waveforms were recorded using a digital oscilloscope at a sampling frequency of 100 MHz (Lecroy 9354 TM; Chestnut Ridge, NY). Although a spherically focused transducer was selected for the evaluation, the experimental techniques can be applied to any focused source including dynamically focused arrays.

The first method considered for determining the Gaussian dimensions was the traditional technique of passing a wire target systematically through the entire ultrasound beam in a water bath and recording the pulse/echo waveform for each field location [*Raum and O'Brien*, 1997]. The wire target is then assumed to approximate a point target (i.e., neglect integration of wire across beam). In order to insure that the correct dimensions were measured, the wire needs to be moved throughout the entire field since it is difficult to align the beam axis with the scan axis when using a wire. In our experiment, the 38-μm-diameter tungsten wire (California Fine Wire Company, Grover City, CA) was moved in a rectangular grid of dimension 10 mm by 1.2 mm in steps of 50 μm and 30 μm, respectively, using a Daedal microprecision positioning system (Daedal Inc., Harrison City, PA). The pulse intensity integral (*PII*) was then calculated for the return echo from every wire location yielding an image of the beam pattern. From the *PII* beam pattern, the beam axis (*z*-axis) and focal plane axis (*x*-axis) were determined. An image showing the log-compressed *PII* beam pattern along with the field axes is shown in Figure 3.7. For arrays or other beams lacking circular symmetry in the focal plane, the experiment would need to be repeated with the wire target rotated so that the field intensity at each frequency along the *y*-axis could also be obtained. Another possibility would be to use a hydrophone to map out the entire three-dimensional field.

Once the field axes were determined, the magnitude of the Fourier transform for each waveform at each location along the axes was calculated yielding the field intensity at each frequency and axial position. The field intensity for frequencies between 7 MHz and 10 MHz versus the location on the field axes was then fit by a Gaussian distribution yielding the appropriate frequency-dependent equivalent Gaussian dimensions. Finally, a linear fit was performed on the measured dimensions versus the acoustic wavelength yielding frequency-

dependent Gaussian dimensions of $w_z = 17.1\lambda + 924 \cdot 10^{-6}$ m and $w_x = 1.57\lambda + 27.0 \cdot 10^{-6}$ m. Plots showing the measured dimensions and the resulting linear fits are shown in Figure 3.8. When λ goes to zero, the beamwidths and depth of focus do not go to zero due to the intercept term. This results from the sources not being ideally diffraction limited.

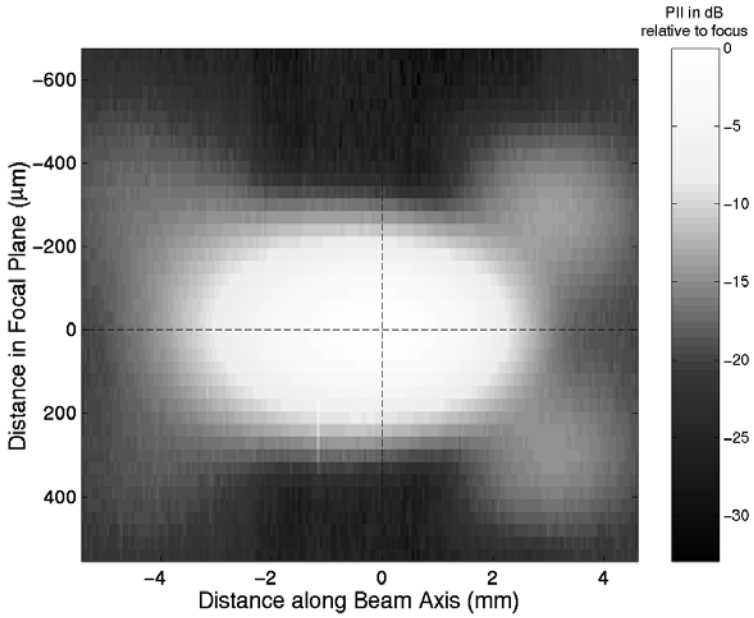

Figure 3.7: Image of *PII* in dB showing location of field axes (dotted line) for the beamwidth measurement from the wire reflections.

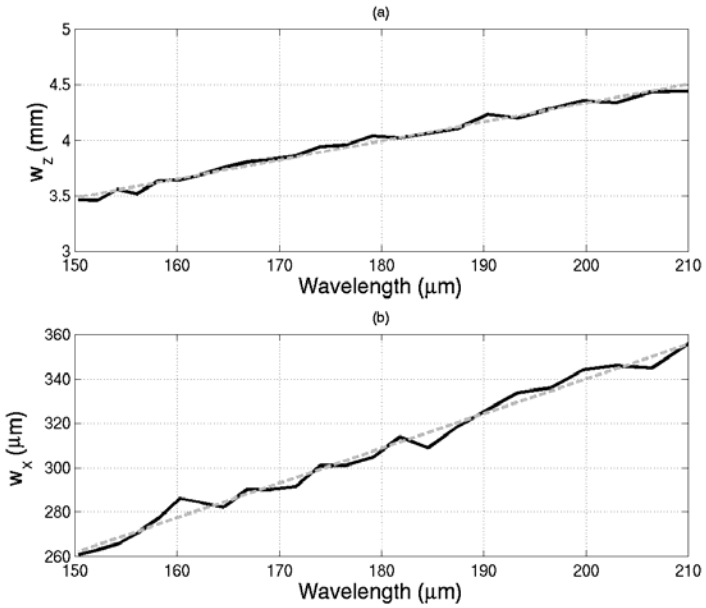

Figure 3.8: Measured beamwidths (solid line) and the resulting linear fits (dashed line) for the beam axis (a) and the focal plane axis (b) from the wire reflections.

The determination of the frequency-dependent Gaussian dimensions of a source using the wire technique is robust. However, it is very time-consuming due to the need to map out most of the acoustic field, a problem that would only be compounded by diagnostically relevant fields with multiple foci. Furthermore, it provides more information than is required (i.e., w_x). In Chapter 2, it was demonstrated that in order to correct for focusing along the beam axis when determining the scatterer size only w_z was needed. Hence, the second method considered for determining the Gaussian dimensions was a faster measurement that only yielded w_z.

The second method used to obtain the equivalent frequency-dependent Gaussian depth of focus is based on the theoretical backscattered signal from a rigid plane positioned near the focal plane given by Equation (2.71) as

$$V_{plane}(\omega) = \frac{-w_x w_y k_o^2 G_o^2 V_{inc}(\omega) H^2(\omega)}{8\pi S_T} e^{i2k_o(z_T - z_f)} e^{-2\left(\frac{z_f}{w_z}\right)^2}. \tag{3.7}$$

A smooth Plexiglas surface was initially positioned 2 mm past the focal plane for the transducer in a water bath (z_f = -2 mm). The Plexiglas surface was then moved along the beam axis passing through the focus in steps of 150 μm until it was 2 mm in front of the focus (z_f = 2 mm) using the Daedal microprecision positioning system, and the echo waveforms were recorded for each Plexiglas location. The magnitude of the Fourier transform was then calculated for each of the acquired waveforms.

The resulting magnitude spectra were then divided by the spectrum obtained for the Plexiglas located at the focal plane (z_f = 0) for frequencies between 7 MHz and 10 MHz and fit by a Gaussian distribution yielding the equivalent Gaussian depth of focus along the beam axis w_z. Then, a linear fit was performed on the measured depths of focus versus wavelength yielding a frequency-dependent Gaussian depth of focus of $w_z = 16.1\lambda + 802 \cdot 10^{-6}$ m which differed by less than 7.6 % from depth of focus found using the wire technique. Therefore, the two methods for measuring the frequency-dependent Gaussian depth of focus along the beam axis w_z are equivalent.

The second method is a simple extension to the calibration method of placing a rigid plane at the focal plane which is currently used to obtain a reference in scatterer size estimates [*Oelze et al.*, 2002; *Lizzi et al.*, 1983; *Insana et al.*, 1990; *Madsen et al.*, 1984]. Due to the reduced measurement time, the measurement of the depth of focus using the rigid plane was also used to determine the w_z values for the other sources used in the phantom experiments. These

values are provided in Table 3.1 along with the scan length the planar reflector was moved when acquiring the reflections. Variations in the scan length did not significantly change the resulting w_z values indicating secondary field properties (i.e., waveform curvature) did not dramatically effect the measured Gaussian depth of focus for the focal region.

Table 3.1: Relevant properties of transducers used in the phantom experiments.

f#	Center Frequency	-3 dB Bandwidth	Transducer Diameter	Scan Length (Step Size) to find w_z	w_z	Depth into Phantom
1	8.7 MHz	1.5 MHz	2.1 cm	-2 mm → 2 mm (50 μm)	$3.22\lambda + 1285$ μm	6 mm
2	8.7 MHz	1.6 MHz	2.1 cm	-2 mm → 2 mm (150 μm)	$16.1\lambda + 802$ μm	12.5 mm
4	9.4 MHz	3.8 MHz	1.4 cm	-8 mm → 8 mm (200 μm)	$76.8\lambda + 4207$ μm	15 mm

3.2.2 Experimental procedure and results

The phantom experiments were designed to validate the use of focused sources in predicting scatterer size as well as investigate the effects of focusing along the beam axis in greater detail. Hence, the three transducers described in Table 3.1 were used to estimate the radius of glass beads in a tissue mimicking phantom. The reported center frequencies and –3 dB bandwidths had been previously measured by a wire reflection technique [*Raum and O'Brien*, 1997].

The agar phantom used in the experiment was produced at the University of Wisconsin and was part of an interlaboratory comparison of ultrasonic backscatter, attenuation, and sound speed measurements [*Madsen et al.*, 1999]. The phantom consisted of degassed water, agar, n-proponal, finely powdered graphite, and glass beads whose radii varied between 22.5 μm and 26.5 μm with an average concentration of 20.454 /mm^3. The attenuation of the phantom (0.55 ± 0.08 dB/cm/MHz) was measured by both insertion loss techniques as well as by observing the change in backscatter with propagation depth into the phantom at room temperature. The sound speed of the phantom was reported by *Madsen et al.* [1999] to have a mean value of 1534.4 m/s at 22 ^{o}C with a temperature dependence of 1.7 m/s/ ^{o}C.

The experiments were performed by first positioning a rigid plane at the focus of the transducer in a degassed water bath. The transducers were shock excited using a Panametrics

5900 pulser/receiver operating in pulse-echo mode, and the echo waveforms were captured using a Lecroy 9354 TM digital oscilloscope with a sampling frequency of 100 MHz. The focus was defined as the plane location that resulted in the largest peak-peak voltage for the returned echo waveform. This echo waveform was then recorded as the reference waveform V_{plane}. The rigid plane used to obtain the reference waveform was made of either Plexiglas or polished metal. The plane was then moved along the beam axis so that the values of w_z could be determined as described previously.

The phantom was then placed such that the reflection from the front surface of the phantom corresponded in time with the previously acquired reference waveform, thereby positioning the front surface of the phantom in the focal plane of the transducer. The focus was then moved into the phantom a known distance by using the Daedal microprecision positioning system. Care was taken so that secondary reflections between the surface of the transducer and the surface of the phantom did not interfere with the speckle from the glass beads. The distance the focus was moved into the phantom for each transducer is also given in Table 3.1.

After positioning the focus, 25 independent RF echoes were acquired by moving the phantom along a square grid parallel to the focal plane using the Daedal microprecision positioning system. The grid consisted of 5 columns and 5 rows each separated by a distance of 450 μm, 450 μm, and 1 mm for the *f*/1, *f*/2, and *f*/4 transducers, respectively. For each grid position, the echo waveform was averaged between 1000 to 2200 times to remove as much electronic noise as possible.

During processing, each RF echo was windowed by a rectangular gating function centered at the focus, the location of which was known from the reference signal. A rectangular gating function was selected because the traditional attenuation compensation functions (A_{OO} and A_{OM}) are defined for a rectangular gate. The positioning was done by measuring the water temperature, calculating the sound speed of the water/phantom medium (c_o and c) from the temperature, and then using these sound speeds to position the window at the correct location in time. The length of the gating functions varied from 1 mm to 13 mm in steps of 0.5 mm with corresponding time gates given by $T_{win} = 2L/c$. After windowing, the magnitude of the Fourier transforms for each RF echo were averaged together yielding an estimate for $\mathrm{E}\left[\left|V_{refl}(\omega)\right|^2\right]$. An estimate for the radius of the glass beads was then obtained by finding the value of a_{eff} that

minimized the average squared difference (*ASD*) given by Equation (2.75). The minimization was done for frequencies in the range of 6.5 MHz to 10.5 MHz for all three of the transducers so that differences in the bandwidth of the transducers would not affect the comparison.

The average value of the glass bead radius for window lengths between 3 mm and 8 mm found using the generalized attenuation compensation function was 26.1 μm, 22.8 μm, and 22.9 μm for the *f*/1, *f*/2, and *f*/4 transducers, respectively. Hence, the estimated bead radii were well within the range of bead radii known to be in the phantom (i.e., 22.5 μm to 26.5 μm). Previously, it was shown that the differences between the different attenuation-compensation functions should be relatively constant between different scatterer distributions even though the absolute errors would vary. Hence, the percent difference between the traditional attenuation-compensation functions and the generalized attenuation-compensation function relative to the mean glass bead radius of 24.5 μm was used in this evaluation.

The percent difference versus window length for each of the transducers is shown in Figure 3.9, and the percent difference versus normalized window length where the window length has been divided by the calculated depth of field for the transducer (i.e., $7.08\lambda_0 f\#^2$) is given in Figure 3.10. The traditional attenuation-compensation functions A_{PC}, A_{OM}, and A_{OO} all predict larger bead sizes than the generalized attenuation-compensation function for the *f*/1 and *f*/2 transducers. Also, for the *f*/4 transducer, A_{PC} gives a smaller estimate while A_{OM} and A_{OO} continue to give larger estimates. This same qualitative behavior was also observed in our earlier simulation study. However, there was not quantitative agreement in the amount of improvement provided by the new generalized attenuation-compensation function.

For the Gaussian scatterers, the generalized attenuation-compensation function gave an improvement in the scatterer size estimate of 40% to 50% over the traditional attenuation-compensation functions for the *f*/2 transducer with a window length of 13 mm and an attenuation of 0.5 dB/cm/MHz. In the experiment, the *f*/2 transducer only gave an improvement of 12% to 18%. Likewise, the improvement in the experiment for the *f*/1 transducer was only about 3.5% to 6% when our previous simulation study with Gaussian scatterers predicted an improvement of 35% to 55%. Theoretically, the experimental difference should have been larger due to the slightly increased attenuation. Also, in the experiments, the *f*/1 transducer yielded improvements in the scatterer size estimate much smaller than the *f*/2 transducer when our previous simulation study seemed to indicate that the differences should plateau at approximately the same values as

the window length is increased for both transducers. Even the *f*/4 transducer had less improvement in the experiment (i.e., 7.1% for A_{OM} at 13 mm) as compared to the simulation study (i.e., 17% for A_{OM} at 13 mm). Clearly, these differences in the improvements in the scatterer size estimate when using A_{comp} in the experiment as compared to the earlier simulations with Gaussian scatterers need to be understood.

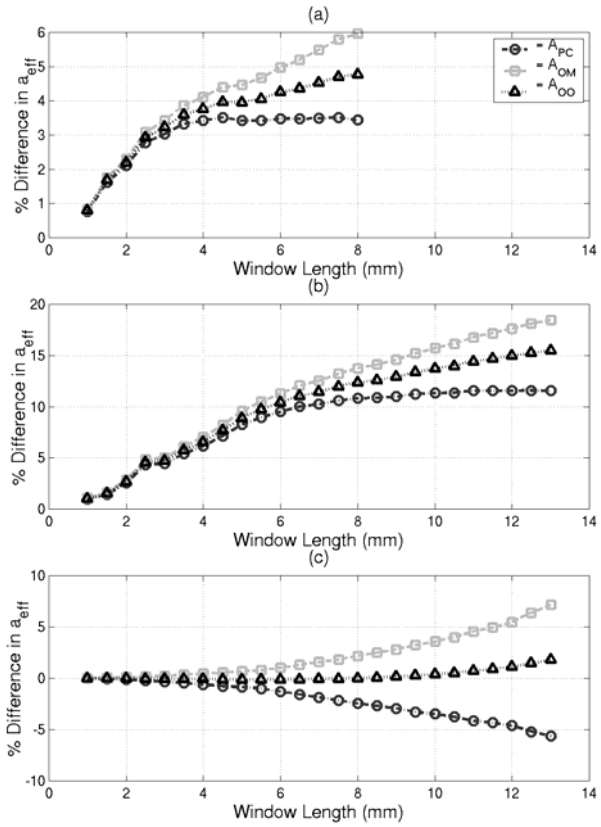

Figure 3.9: Experimental results for percent difference in a_{eff} versus window length found using traditional attenuation compensation functions as compared to a_{eff} found using A_{comp} for a glass bead phantom with an attenuation of 0.55 ± 0.08 dB/cm/MHz, a concentration of 20.454 beads/mm^3, and a mean bead radius of 24.5 μm from spherically focused transducers with f-numbers of (a) *f*/1, (b) *f*/2, and (c) *f*/4.

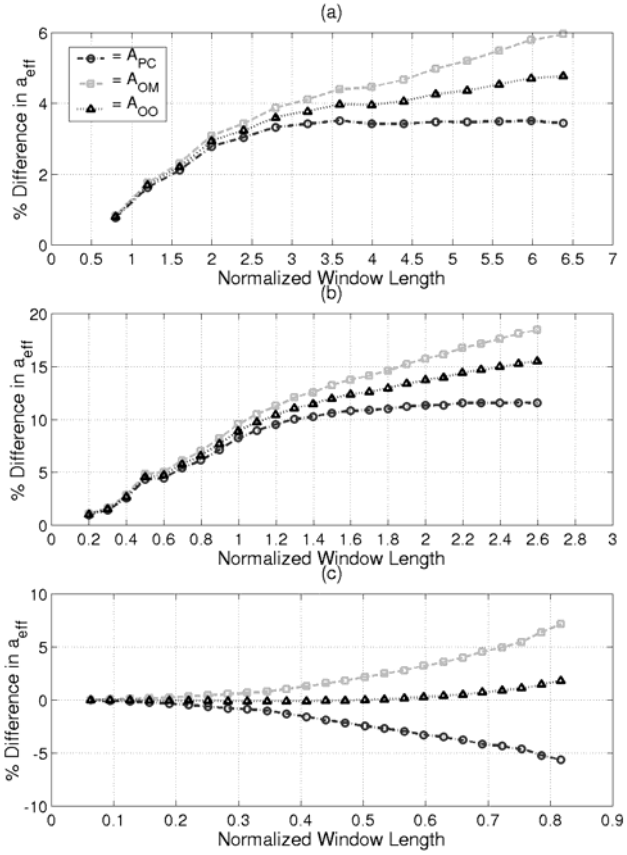

Figure 3.10: Experimental results for percent difference in a_{eff} versus normalized window length found using traditional attenuation compensation functions as compared to a_{eff} found using A_{comp} for a glass bead phantom with an attenuation of 0.55 ± 0.08 dB/cm/MHz, a concentration of 20.454 beads/mm^3, and a mean bead radius of 24.5 μm from spherically focused transducers with f-numbers of (a) *f*/1, (b) *f*/2, and (c) *f*/4.

3.3 Simulation Results for Glass Bead Scatterers

The most obvious difference between the previous simulation study and the experimental study is the type of scatterer. The earlier simulation study used Gaussian scatterers whereas the experimental study used glass beads. The power spectral density function (or form factor) for these two types of scatterers are very different [*Insana et al.*, 1990]. Specifically, the form factor approximating the glass bead falls off much faster with increasing scatterer radius than does the Gaussian scatterer [*Insana et al.*, 1990]. As a result, errors in the minimization routine due to errors in the attenuation-compensation function are less significant when estimating the size of the glass beads. This would result in a decrease in the improvement provided by the new attenuation-compensation function.

In order to test whether the use of glass beads instead of Gaussian scatterers was responsible for the loss in improvement between the earlier simulation study and the experimental study, some simulations were run using glass beads for the scatterers. However, the sources were still assumed to be diffraction limited with velocity potential fields with a three-dimensional Gaussian distribution at the focus. Hence, w_z was given by $6.01\lambda f\#^2$, and $w_{x,y}$ was given by $w_x = w_y = 0.87\lambda f\#$. In the new simulations, the attenuation, sound speed, and scatterer concentration were set to the values determined for the phantom. Likewise, the radius of the shells was set at 24.5 μm. Once again, 1000 independent scatterer distributions were generated and then processed in groups of 25 to yield 40 independent estimates for the scatterer size.

The simulated sources were also excited by an impulse spike (to model the Panametrics pulse) and had Rayleigh frequency responses found by fitting a Rayleigh distribution (i.e., $|f| \cdot \exp\left(-\left(\frac{f - f_R}{\sigma_R} \right)^2 \right)$) to the measured frequency spectrum from the reflection off of the rigid plane at the focus. This was done so that the resulting spectrum of the simulated sources would be as close as possible to the real sources. The bandwidth used in the estimate, however, consisted of the frequencies in the range between 6.5 MHz and 10.5 MHz as was done for the experimental results. Other source parameters, including the depth at which the focus was placed in the simulated phantom, were identical to those provided in Table 3.1.

A plot showing the simulated phantom results is given in Figure 3.11. The differences between the different attenuation-compensation functions are greatly reduced. For the *f*/4 transducer at a window length of 13 mm, the difference between the size estimate given by A_{OM} and A_{comp} is 6.4 % compared to 7.1% for the experimental results. Likewise, A_{OO} and A_{PC} gave simulated differences of 2.9% and –1.75%, respectively, comparable to the experimental differences of 1.8% and –5.6%. Similarly, the *f*/2 transducer at a window length of 13 mm gave simulated differences of 18% for A_{OM}, 15.6% for A_{OO}, and 12.4% for A_{PC} that were very close to the differences of 18.4%, 15.5% and 11.5%, respectively, that were found experimentally. Therefore, the decrease in improvement discussed previously (i.e., % difference of 12% to 18% instead of 40% to 50% for the *f*/2) can be directly attributed to the type of scatterer being measured.

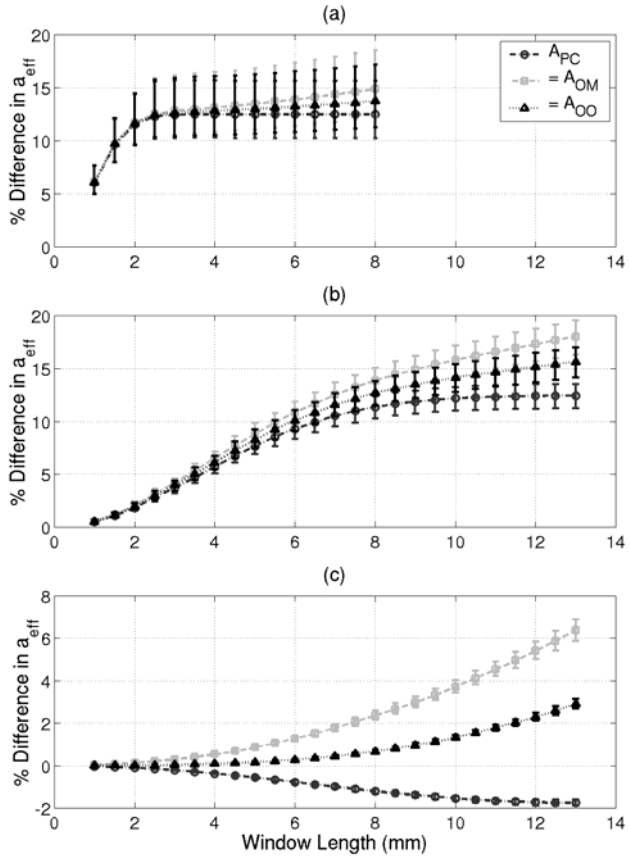

Figure 3.11: Simulation results for percent difference in a_{eff} found using traditional attenuation compensation functions as compared to a_{eff} found using A_{comp} for a glass bead phantom with an attenuation of 0.55 ± 0.08 dB/cm/MHz, a concentration of 20.454 beads/mm^3, and bead radius of 24.5 μm from spherically focused transducers with f-numbers of (a) *f*/1, (b) *f*/2, and (c) *f*/4, and $w_z = 6.01\lambda f\#^2$.

The influence of scatterer type on the improvement provided by the generalized attenuation-compensation function is of great importance for estimating scatterer sizes of biological tissue because the fundamental scatterer geometry (type) in tissue has not been determined. Hence, the improvement of the new generalized attenuation-compensation function compared to the traditional attenuation-compensation functions may be even more significant in a clinical setting because the correct scatterer geometry may exhibit an even stronger dependence on the attenuation-compensation function.

Although the type of scatterer and the subsequent dependence on the attenuation-compensation function explains the reduction in the improvement provided by the new attenuation-compensation function, it does not explain why the plateau of the *f*/1 transducer (i.e.,

difference for A_{PC} of 3.4 %) was different than the plateau for the *f*/2 transducer (i.e., difference for A_{PC} of 11.5 %). Both of the previous simulation studies showed them converging to the same value whereas in the experiment they converged to different amounts of improvement. In order to understand this behavior, another difference between the Gaussian simulation study and the experimental study was explored, namely the wavelength dependence of the effective Gaussian beamwidth along the beam axis, w_z. In the earlier simulations, w_z was directly proportional to the wavelength (i.e., $w_z = 6.01(f\#)^2 \cdot \lambda$), but in the experiment, w_z had the form

$$w_z = w_{zm} \cdot \lambda + w_{zb} \tag{3.8}$$

where w_{zb} was a constant independent of wavelength (Table 3.1).

In order to understand the impact of the wavelength dependence of w_z, the curves of $\ln(A_{comp}/A_{OM})$ and $\ln(A_{comp}/A_{PC})$ versus frequency were fit by a line. The slope of this line could then be used to predict how the scatterer size estimate from A_{comp} would compare to the estimate from A_{OM} and A_{PC}. A positive slope means that the estimate from $A_{PC/OM}$ is larger than the estimate obtained from A_{comp}. Likewise, a negative slope means that the estimate from $A_{PC/OM}$ is smaller than the estimate from A_{comp}. The wavelength dependence of w_z was evaluated for three different w_z values: (a) $6.01(f\#)^2 \cdot \lambda$, as was used in the previous simulation studies, (b) $6.01(f\#)^2 \cdot \lambda + 1285 \ \mu\text{m}$, similar to the wavelength dependence found for the measured transducers, and (c) $6.01(f\#)^2 \cdot (181 \ \mu\text{m})$. The calculations were performed for window lengths normalized to the traditional depth of focus (i.e., $7.08\lambda_0 f\#^2$) of 0.5, 1, and 2.5 as well as for a window length of 8 mm. The resulting slopes are shown in Figures 3.12 and 3.13.

Consider first the w_z values of $6.01(f\#)^2 \cdot \lambda$ shown by the solid curves. For any given normalized window length, the A_{OM} estimate is larger than the A_{comp} estimate and increases with increasing f-number. Likewise, the A_{PC} estimate is larger than the A_{comp} estimate for smaller f-numbers and then decreases with increasing f-number for smaller normalized window lengths resulting in the A_{PC} estimate being smaller than the A_{comp} estimate. For larger normalized window lengths, the A_{PC} estimate is always larger than the A_{comp} estimate and there is no longer any dependency on f-number corresponding to the plateau observed earlier.

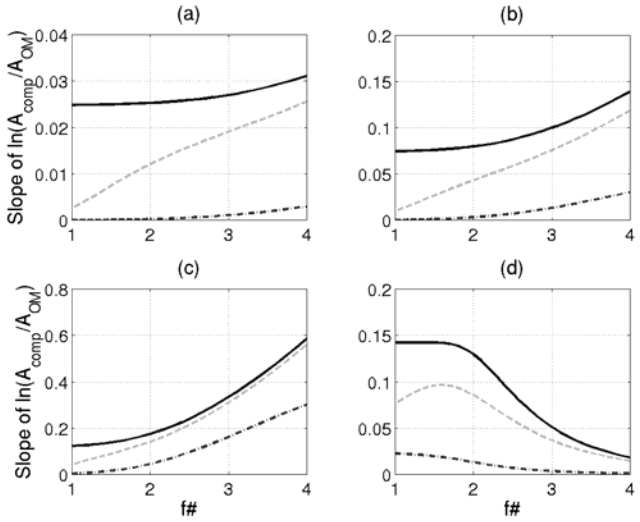

Figure 3.12: Calculated slope of $\ln\left(A_{comp}/A_{OM}\right)$ versus frequency for transducers with varying degrees of focusing (i.e., *f*#). The three curves in the plots correspond to w_z values with three different dependencies on wavelength; ▬ for $w_z = 6.01\left(f\#\right)^2 \cdot \lambda$, ▬ ▬ for $6.01\left(f\#\right)^2 \cdot \lambda + 1285 \ \ \mu\text{m}$, and ▬ ▪ ▬ for $6.01\left(f\#\right)^2 \cdot \left(181 \ \ \mu\text{m}\right)$. The plots had (a) normalized window length of 0.5, (b) normalized window length of 1, (c) normalized window length of 2.5, and (d) window length of 8 mm.

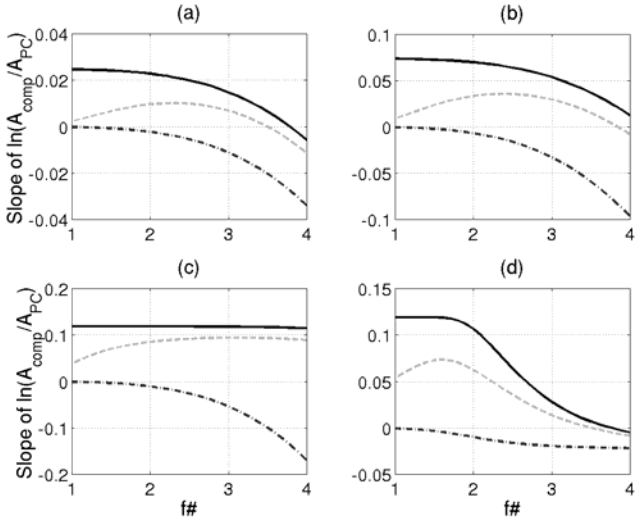

Figure 3.13: Calculated slope of $\ln\left(A_{comp}/A_{PC}\right)$ versus frequency for transducers with varying degrees of focusing (i.e., *f*#). The three curves in the plots correspond to w_z values with three different dependencies on wavelength; ▬ for $w_z = 6.01\left(f\#\right)^2 \cdot \lambda$, ▬ ▬ for $6.01\left(f\#\right)^2 \cdot \lambda + 1285 \ \ \mu\text{m}$, and ▬ ▪ ▬ for $6.01\left(f\#\right)^2 \cdot \left(181 \ \ \mu\text{m}\right)$. The plots had (a) normalized window length of 0.5, (b) normalized window length of 1, (c) normalized window length of 2.5, and (d) window length of 8 mm.

Consider now the w_z values illustrated by the remaining curves. The sizes of the $A_{PC/OM}$ estimates relative to the size of the A_{comp} estimate are reduced as the wavelength dependency of w_z is reduced as is illustrated by the dash-dot-dash curve ($6.01(f\#)^2 \cdot \lambda + 1285 \ \ \mu\text{m}$) being lower than the dashed curve ($6.01(f\#)^2 \cdot (181 \ \ \mu\text{m})$). Also, for w_z given by $6.01(f\#)^2 \cdot \lambda + 1285 \ \ \mu\text{m}$, the estimates approach the $6.01(f\#)^2 \cdot \lambda$ curve for larger f-number and approach the $6.01(f\#)^2 \cdot (181 \ \ \mu\text{m})$ curve for smaller f-number. As a result, the A_{PC} estimates no longer plateau independent of f-number. Therefore, the *f*/1 transducer used in the experiment should have yielded a smaller difference between the A_{PC} and A_{comp} estimates than the *f*/2 transducer, just as was observed, due to its weaker dependence on wavelength.

The results for A_{PC} as compared to A_{comp} at large normalized window lengths can also be shown mathematically. For sufficiently large window lengths, the integral along the beam axis in A_{comp} can be evaluated in closed form yielding

$$A_{comp}(\omega) = \frac{2}{w_z\sqrt{\pi}} \mathrm{e}^{4\alpha z_T} \, e^{-\alpha_1^2 w_z^2}. \tag{3.9}$$

Hence, the derivative of $\ln\left(A_{comp}/A_{PC}\right)$ versus frequency is given by

$$\frac{\partial}{\partial f}\left\{\ln\left(\frac{A_{comp}}{A_{PC}}\right)\right\} = -\frac{1}{w_z}\frac{\partial w_z}{\partial f} - 2(\alpha_1 w_z)\left[w_z \frac{\partial \alpha_1}{\partial f} + \alpha_1 \frac{\partial w_z}{\partial f}\right] \tag{3.10}$$

which can be simplified to

$$\frac{\partial}{\partial f}\left\{\ln\left(\frac{A_{comp}}{A_{PC}}\right)\right\} = \frac{w_{zm} c\left(f^{-2}\right)}{w_{zm}\cdot\lambda + w_{zb}} + \left[2\alpha_1^2\left[w_{zm}\cdot\lambda + w_{zb}\right]w_{zm} c\left(f^{-2}\right) - 2\alpha_1\left[w_{zm}\cdot\lambda + w_{zb}\right]^2 \frac{\partial \alpha_1}{\partial f}\right] \tag{3.11}$$

if w_z has the form given in Equation (3.8). Hence, the significance of the wavelength dependence of w_z is also affected by the magnitude and frequency dependence of the attenuation. For the purpose of comparison, the attenuation will be assumed to have a strict linear frequency dependence (i.e. $\alpha_1 = \alpha_o \cdot f$) allowing Equation (3.11) to be rewritten as

$$\frac{\partial}{\partial f}\left\{\ln\left(\frac{A_{comp}}{A_{PC}}\right)\right\} = \frac{1}{f}\left(\frac{w_{zm}\cdot\lambda}{w_{zm}\cdot\lambda + w_{zb}}\right) - 2\alpha_o^2 f w_{zb}\left[w_{zm}\cdot\lambda + w_{zb}\right]. \tag{3.12}$$

Hence, if w_{zb} = 0, then the slope of $\ln\left(A_{comp}/A_{PC}\right)$ versus frequency is equal to 1/*f* and is independent of the value of w_{zm}. Likewise, if w_{zm} = 0, then the slope of $\ln\left(A_{comp}/A_{PC}\right)$ versus

frequency decreases approximately parabolically with increasing values of w_{zb}. Both of these effects are evident in Figure 3.13c.

The impact of the wavelength dependence of w_z on the different attenuation-compensation functions was further tested by repeating the simulation of the glass bead phantoms using the w_z values found experimentally. Once again, the attenuation, sound speed, and scatterer concentration were set to the values determined for the phantom, and the radius of the shells was set at 24.5 μm. Also, 40 independent estimates were obtained for 1000 independent scatterer distributions that were generated and then processed in groups of 25 using frequencies in the range between 6.5 MHz and 10.5 MHz. The simulated sources were also modeled to have the same Rayleigh frequency response as was found experimentally and were excited by an impulse spike. The resulting differences between the different attenuation-compensation functions are shown in Figure 3.14. Once the measured values for w_z were used in the simulations, the differences between the attenuation-compensation functions for the *f*/1 transducer at 8 mm were 7.4%, 5.9%, and 4.3% whereas the differences for the *f*/2 transducer at 13 mm were 16%, 13.4%, and 10% for A_{OM}, A_{OO}, and A_{PC}, respectively. Hence, A_{PC} for the *f*/1 transducer and the *f*/2 transducer now plateau at different levels in agreement with the observed experimental results. Therefore, the wavelength dependence of w_z was responsible for their earlier discrepancy. Furthermore, the differences found experimentally and the mean differences found in the simulations using the correct value for w_z were consistently within 2.5% of each other, validating the theoretical analysis provided in Chapter 2.

3.4 Chapter Summary

In this chapter, the use of focused sources for estimating scatterer sizes was investigated through simulation studies and phantom experiments. First, simulation studies with Gaussian scatterers demonstrated that including the effects of diffraction along the beam axis improves the accuracy of the scatterer size estimator even for a weakly focused *f*/4 transducer. The improvement in accuracy for the more strongly *f*/1 and *f*/2 transducers was on the order of 20% to 100% depending on the length of the window and the amount of attenuation.

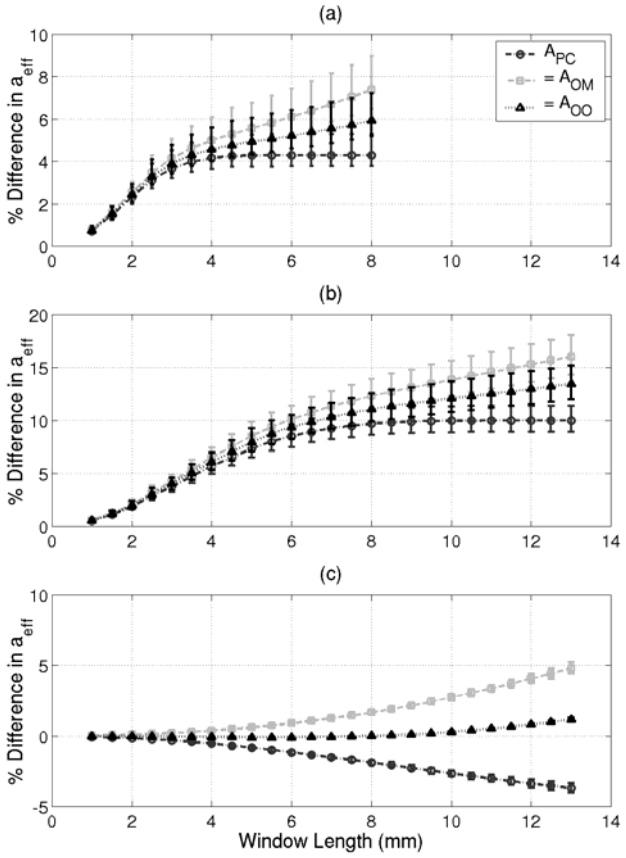

Figure 3.14: Simulation results for percent difference in a_{eff} found using the traditional attenuation-compensation functions as compared to a_{eff} found using A_{comp} for a glass bead phantom with an attenuation of 0.55 ± 0.08 dB/cm/MHz, a concentration of 20.454 beads/mm^3, and bead radius of 24.5 μm from spherically focused transducers with f-numbers of (a) *f*/1, (b) *f*/2, and (c) *f*/4, and w_z as given in Table 3.1.

Then, two different methods for measuring the equivalent Gaussian dimensions for a focused source were compared. It was determined that simply recording/processing the echoes from a rigid plane moved along the beam axis could yield sufficient calibration information. Then, real focused transducers were used to estimate the size of glass beads in a tissue-mimicking phantom and compared to simulation studies with glass beads. The simulations and phantom experiments had agreement better than 2.5% provided that the same type of scatterers and sources were being compared. Errors in the attenuation-compensation function when estimating the radius of the glass beads were much less significant than the same errors when estimating the radius of a Gaussian scatterer due to the stronger frequency dependence of the form factor for the glass bead scatterer. Lastly, the effects of focusing were explored in greater

detail, and it was found that the improvement provided by the new generalized attenuation-compensation function decreased as the wavelength dependence of w_z was reduced.

Before concluding, recall that the theoretical derivations in Chapter 2 neglected multiple scattering. This is the traditional approximation made when performing this type of analysis [*Insana et al.*, 1990] due to the weak scattering and large attenuation of biological tissue. The good agreement between the real phantom experiments and computer simulations demonstrate that multiple scattering is not important for this application and need not be considered in the remaining simulations provided in this thesis.